

Quantum technologies with optically interfaced solid-state spins

Awschalom, David D.; Hanson, Ronald; Wrachtrup, Jörg; Zhou, Brian B.

DOI

[10.1038/s41566-018-0232-2](https://doi.org/10.1038/s41566-018-0232-2)

Publication date

2018

Document Version

Accepted author manuscript

Published in

Nature Photonics

Citation (APA)

Awschalom, D. D., Hanson, R., Wrachtrup, J., & Zhou, B. B. (2018). Quantum technologies with optically interfaced solid-state spins. *Nature Photonics*, 12(9), 516-527. <https://doi.org/10.1038/s41566-018-0232-2>

Important note

To cite this publication, please use the final published version (if applicable). Please check the document version above.

Copyright

Other than for strictly personal use, it is not permitted to download, forward or distribute the text or part of it, without the consent of the author(s) and/or copyright holder(s), unless the work is under an open content license such as Creative Commons.

Takedown policy

Please contact us and provide details if you believe this document breaches copyrights. We will remove access to the work immediately and investigate your claim.

1 **Quantum Technologies with Optically Interfaced Solid-State Spins**

2 David D. Awschalom^{1,2,†}, Ronald Hanson^{3,4}, Jörg Wrachtrup^{5,6}, Brian B. Zhou^{1,*}

3 ¹ *Institute for Molecular Engineering, University of Chicago, Chicago, Illinois 60637, USA*

4 ² *Institute for Molecular Engineering and Materials Science Division, Argonne National*
5 *Laboratory, Argonne, Illinois 60439, USA*

6 ³ *QuTech, Delft University of Technology, P. O. Box 5046, 2600 GA Delft, The Netherlands*

7 ⁴ *Kavli Institute of Nanoscience, Delft University of Technology, P. O. Box 5046, 2600 GA Delft,*
8 *The Netherlands*

9 ⁵ *Institute for Quantum Science and Technology IQST, and 3. Physikalisches Institut, University*
10 *of Stuttgart, Pfaffenwaldring 57, 70569 Stuttgart, Germany*

11 ⁶ *Max Planck Institute for Solid State Research, Heisenbergstraße, 1 70569 Stuttgart, Germany*

12 ^{*} *Present address: Department of Physics, Boston College, Chestnut Hill, Massachusetts*
13 *02467, USA*

14 [†] email: awsch@uchicago.edu

15

16 **Spins of impurities in solids provide a unique architecture to realize quantum**
17 **technologies. A quantum register of electron and nearby nuclear spins in the lattice**
18 **encompasses high-fidelity state manipulation and readout, long-lived quantum memory,**
19 **and long-distance transmission of quantum states by optical transitions that coherently**
20 **connect spins and photons. These features, combined with solid-state device engineering,**
21 **establish impurity spins as promising resources for quantum networks, information**
22 **processing, and sensing. Focusing on optical methods for the access and connectivity of**
23 **single spins, we review recent progress in impurity systems such as color centers in**
24 **diamond and silicon carbide, rare-earth ions in solids, and donors in silicon. We project a**
25 **possible path to chip-scale quantum technologies through sustained advances in**
26 **nanofabrication, quantum control, and materials engineering.**

27

28 Driven by the quest for efficiency, modern technologies developed through persistent
29 miniaturization. Devices such as transistors, magnetic memories, and lasers advanced by
30 reducing the number of electrons used per gate, bit, or output photon. This progression's arrival
31 at the quantum limit now inspires a new class of information processing hardware that starts with
32 the quantum coherence of single charges, spins, or photons and grows by harnessing the
33 inseparable connections among them. This reversal from scaling down to building up lies at the

34 heart of radical technologies that promise breakthroughs in computational power,
35 communications security, and sensor detection limit.

36 Solid-state spins are a promising platform for realizing these quantum advantages
37 because of their robustness to decoherence and compatibility with scalable device engineering¹.
38 In particular, this review focuses on optically addressed electron and nuclear spins at impurities
39 in crystals. In recent years, pioneering experiments have isolated single spins at these atomic-
40 scale impurities and demonstrated high-fidelity initialization, manipulation, and readout of their
41 quantum states². These advances at the single-qubit level establish a critical foundation, but the
42 connectivity among multiple qubits is required to unlock their full potential. We highlight the
43 capacity of hybrid quantum registers formed by an electron spin coupled to multiple nuclear spins
44 in its proximity. Electron spins readily sense and interface to the outside environment, while
45 nuclear spins provide well-isolated quantum memories. These complementary functionalities,
46 accessed through the generation of entangled states, enable an array of applications, including
47 photonic memories³, quantum repeaters⁴, error-correction⁵, and enhanced quantum sensing⁶.

48 We concentrate on solid-state spins that utilize optical electronic transitions to fulfill several
49 of the DiVincenzo criteria for quantum information processing⁷. Optical pumping can directly
50 initialize the electron spin and its coupled nuclear spins, or alternatively, coherent manipulations
51 can transfer optically generated electron spin polarization to nuclear memories^{8,9}. Additionally,
52 spin-dependent optical cycles correlate spin information to photon emission, enabling sensitive
53 readout of spin states. Such remarkable optical properties of defect systems have been combined
54 with techniques adapted from atomic physics and magnetic resonance to empower experiments
55 on single electron and nuclear spins at ambient conditions, surpassing limitations in the original
56 fields. Moreover, spin-selective optical transitions, accessed at cryogenic temperatures,
57 coherently map between the quantum states of local spins and propagating photons^{10,11}. This
58 light-matter interface establishes each electron as a quantum gateway to distribute and process
59 entanglement between distant registers in a quantum network.

60 We aim to provide an introduction and broad update on optically-active impurity systems,
61 emphasizing the partnership between electron and nuclear spins. We first describe the framework
62 for manipulating hybrid quantum registers in the context of the prototype defect system, the
63 nitrogen-vacancy (NV) center in diamond⁸. We briefly review the optical and coherence properties
64 of the NV electron spin, which provides access to the entire register. This discussion identifies
65 the nuclear spin bath as the dominant source of decoherence but leads to the opportunity to

66 control selected nuclear memories via their distinct hyperfine interaction. We then overview
67 emerging impurity systems, including alternative color centers in diamond and silicon carbide,
68 rare-earth ions in solids, and optically-active donors in silicon. These platforms offer unique
69 advantages, such as in their optical properties or integrability with electronic or photonic devices
70 and stand to benefit from techniques developed for the NV center. In a latter part, we focus on
71 technological applications of registers of quantum memories, ranging from quantum
72 communication, computing, and sensing. We conclude our review by looking ahead to future
73 challenges and progress with impurity spins in solids.

74 We remark that spins in self-assembled^{12,13} and gate-defined quantum dots¹⁴ share many
75 parallel directions with impurity spins, including achievement of extended coherence times and
76 enhanced light-matter coupling to enable multi-qubit scaling and single photon nonlinearities. The
77 rapidly advancing state-of-the-art in this field is however beyond the scope of our discussion.
78 Likewise, we will overlook two-dimensional material systems, such as transition metal
79 dichalcogenides and hexagonal boron nitride, that have recently emerged as hosts for single
80 quantum emitters¹⁵⁻¹⁷. For these materials, explorations toward using the valley or spin degree of
81 freedom of excitons or defect states as qubits are still in their infancy but could open functionalities
82 for quantum photonics, optoelectronics, and sensing unattainable in bulk materials.

83 **The NV center in diamond**

84 Consisting of a substitutional nitrogen impurity adjacent to a missing carbon atom, the negatively
85 charged NV center in diamond traps six electrons at localized atomic-like states, protected from
86 charge scattering by diamond's wide bandgap (Fig. 1a). NV centers display room-temperature
87 quantum coherence, spin-photon entanglement, and functionality inside engineered
88 nanostructures, establishing their versatility for quantum information processing and nanoscale
89 sensing.

90 **The electron spin and its optical interface.** The NV electron spin can be off-resonantly excited
91 from its spin-triplet ground state (GS) to a spin-triplet, orbital-doublet excited state (ES) via
92 phonon-assisted optical absorption⁸. Due to a nonradiative, spin-flip decay channel that
93 preferentially couples to the $m_s = \pm 1$ sublevels of the excited state, repeated optical cycling
94 initializes the electron spin into the $m_s = 0$ level (~90% polarization)¹⁸. Concurrently, off-resonant
95 excitation of $|m_s = \pm 1\rangle$ results in ~30% lower photoluminescence (PL) than $|m_s = 0\rangle$, allowing
96 optical determination of the spin state at room temperature¹⁹. Higher fidelity initialization and
97 readout are obtained by cooling diamond below 10 K, where distinct spin-selective, zero-phonon

98 optical transitions are resolved¹⁸ (Fig. 1b). Resonant optical pumping of a spin-mixed transition
99 (e.g. $|m_s = \pm 1\rangle \rightarrow |A_1\rangle$) fully initializes the NV into $|m_s = 0\rangle$ (>99.7% polarization)¹⁸. Alternatively,
100 by resonant excitation of a cycling transition ($|m_s = 0\rangle \rightarrow |E_x\rangle$ or $|E_y\rangle$) and optimizing photon
101 collection efficiency, the electron spin state can be determined without averaging multiple
102 preparations (>97% fidelity averaged for $|m_s = 0\rangle$ and $|m_s = \pm 1\rangle$)²⁰. Such single-shot
103 measurements can be non-demolition to allow initialization of electron and nuclear spins by
104 projective measurement¹⁸. Moreover, these spin-dependent optical transitions and their
105 polarization selection rules form the basis for spin-photon entanglement^{10,11}.

106 Aided by diamond's high Debye temperature and low spin-orbit coupling, NV centers possess
107 long spin-lattice relaxation times T_1 that reach ~5 ms at room temperature and exceed hours at
108 cryogenic temperatures (~25 mK)^{21,22}. In high quality samples grown by chemical vapor
109 deposition, low concentrations of paramagnetic impurities leave the bath of ¹³C nuclear spins
110 (1.1% natural abundance) as the dominant magnetic noise¹⁹. This dephasing can be mitigated in
111 isotopically enriched materials (>99.99% ¹²C). For single spins in isotopically purified samples,
112 the inhomogeneous dephasing time T_2^* , reflecting temporal magnetic fluctuations, exceeds 100
113 μ s at room temperature²³. Dynamical decoupling further filters the noise spectrum and extends
114 spin coherence to the homogeneous dephasing time T_2 of several milliseconds at room
115 temperature²⁴ and nearly seconds at low temperature, limited by direct lattice contributions to spin
116 dephasing ($T_2 \approx 0.5 T_1$)²⁵ (Fig. 1c). These remarkable coherence times underpin the technological
117 promise of NV centers, extending the range of its access to nearby nuclear spins and enhancing
118 its sensitivity to environmental influences.

119 **Strongly-coupled nuclear spins.** While the nuclear bath represents the main contribution to
120 electron spin decoherence, individual nuclear spins with isolated interactions offer a resource for
121 quantum memories and multi-qubit entanglement^{9,26,27}. Strongly-coupled nuclear spins, such as
122 the intrinsic N forming the NV center and proximal ¹³C atoms, possess hyperfine couplings larger
123 than the electron spin resonance (ESR) linewidth, set by the dephasing rate $1/T_2^*$ (Fig. 1a,d). For
124 samples with natural isotope abundance, strongly-coupled nuclei typically occur within 1 nm from
125 the electron and have hyperfine couplings from 300 kHz to 130 MHz, where the latter value
126 corresponds to a ¹³C on a nearest neighbor lattice site²⁸. For these nuclei, narrowband microwave
127 (MW) pulses at the distinct ESR transition frequencies (Fig. 1d) perform rotations of the electron
128 spin conditional on the nuclear spin state (e.g., controlled NOT gate, $C_n\text{NOT}_e$). Moreover, radio-
129 frequency (RF) pulses can directly drive nuclear spin transitions ($\Delta m_I = \pm 1$) conditional on the
130 electron spin manifold (e.g. $C_e\text{NOT}_n$)²⁹. Nuclear rotations can alternatively be implemented by

131 nuclear Larmor precession for orthogonal nuclear quantization axes in different electron
132 manifolds⁹. Using tailored pulse sequences of controlled two-qubit operations, the electron
133 polarization can be transferred to the nuclear spin, after which the electron spin is reset by optical
134 pumping^{9,30}.

135 Readout of the nuclear spin is achieved by mapping its population and coherences onto the
136 electron spin using a combination of selective RF and MW pulses²⁶. In Ref. [31], single-shot
137 readout of the nuclear spin at room temperature was demonstrated by repeated application of
138 electron-nuclear correlation ($C_n\text{NOT}_e$) and optical readout of the electron (Fig. 1e). This repetition
139 leverages the robustness of the nuclear spin to optical excitation to accumulate sufficient photon
140 statistics. Projective readout can initialize multiple strongly coupled nuclei if the $C_n\text{NOT}_e$ logic is
141 conditional on each nuclear spin state of the multi-qubit register¹⁸.

142 The coherence times of nuclear spins and their sensitivity to optical illumination determine their
143 usefulness as quantum memories. Nuclear coherence times T_{2n} exceed several milliseconds at
144 room temperature and are limited by the electron spin relaxation time T_1 and interactions with
145 other nuclei⁹. Control over the NV charge state, either by strong optical illumination³² or
146 electrostatic gating³³, can effectively decouple or eliminate the electron spin, extending nuclear
147 T_{2n} beyond several seconds by the former technique. For nuclear depolarization (T_{1n}), transverse
148 components of the hyperfine interaction drive electron-nuclear flip-flops. Since hyperfine
149 interactions may be stronger in the excited state, optical excitation can exacerbate depolarization,
150 requiring high magnetic fields to minimize this process for strongly-coupled nuclear spins³¹. In
151 addition, these transverse terms become dominant near the excited-state anti-crossing ($B \approx$
152 500 G), enabling optical excitation to drive dynamic nuclear spin polarization (DNP)^{34,35}. The DNP
153 efficiency can approach unity, depending on the strength and direction of the hyperfine
154 interaction³⁶. For quantum networks and error-corrected quantum computing, the coherences of
155 nuclear spins must also be conserved under all operations performed with the electron spin³⁷.
156 Failed remote entanglement attempts due to photon loss or errors in the electron spin readout
157 randomize the electron spin, introducing an uncertainty to the nuclear memory's precession
158 frequency and accumulated phase that cannot be refocused. Hence, these considerations have
159 motivated the exploration of more distant nuclear memories that are less sensitive to electronic
160 interference.

161 **Weakly-coupled nuclear spins.** Access to nuclear spins with hyperfine couplings weaker than
162 $1/T_2^*$ greatly increases the available number of register qubits and improves the longevity of each

163 memory, at the tradeoff of slower control speeds. This objective was achieved using dynamical
164 decoupling (DD) sequences on the electron, thereby both extending its coherence and isolating
165 its interaction with a particular nuclear spin^{23,38,39}. The precession axis and frequency of a nuclear
166 spin is conditional on the electron spin state and on its distinct hyperfine tensor (Fig. 1f). DD
167 pulses that invert the electron spin thus modulate the nuclear precession, such that when the
168 unique dynamics of a targeted nuclear spin is in resonance with the periodicity of the DD pulses,
169 the precession due to its transverse hyperfine component accumulates^{38,40} (Fig. 1g). Meanwhile,
170 destructive interference occurs for nuclear spins with dynamics out-of-sync with the DD sequence.
171 Through this method, universal control⁴⁰ and single-shot readout⁴¹ of weakly-coupled nuclear
172 spins were demonstrated (Fig. 1h). These capabilities, together with remote electron
173 entanglement^{11,42}, establish an architecture for distributed quantum communication and
174 computing based on error-corrected, few-qubit nodes. Moreover, the direct applicability of DD
175 methods to sensing nuclear species external to diamond has impacted progress in nanoscale
176 magnetic resonance^{43,44}.

177 **Emerging Systems for Spin-Light Interfaces**

178 Although possessing long spin coherence, NV centers are hindered by their broad emission
179 spectrum, where only ~4% of the total photons are coherently emitted into the zero-phonon line
180 (ZPL) at 6 K⁴⁵. Since entanglement protocols require indistinguishable photons from remote NVs,
181 this low percentage and the high scattering losses in optical fiber at the ZPL wavelength (637 nm)
182 have limited entanglement rates to 40 Hz²⁰. Achieving higher bandwidth in NV-based quantum
183 networks will thus require photonic cavities to boost ZPL emission⁴⁵⁻⁴⁸ and, for long-distance
184 networks, quantum frequency conversion into telecom wavelengths⁴⁹, together with the
185 advantages of a quantum repeater architecture. Promising for quantum network applications at
186 cryogenic temperatures, recent experiments using microcavities have shown emission into the
187 ZPL with 46% probability⁵⁰, and conversion of single NV photons into telecom wavelength has
188 been reported with 17% efficiency⁵¹. A parallel approach that may alleviate these requirements is
189 the advancement of alternative color centers with more favorable intrinsic properties.

190 **Silicon- and Germanium-Vacancy Centers in Diamond.** The silicon-vacancy center (SiV) in
191 diamond, consisting of an interstitial silicon atom midway between two adjacent carbon vacancies,
192 has garnered interest as a higher efficiency source of indistinguishable photons. The negative
193 charge state SiV⁻ features an orbital doublet in both the ground and excited states, with
194 degeneracies broken by the spin-orbit interaction^{52,53} (Fig. 2a). Four zero-phonon optical

195 transitions between these orbital levels comprise over 70% of the total fluorescence emission,
196 with ~50% into the single line C at 4 K (Fig. 2b). Moreover, due to the defect's inversion symmetry,
197 SiV⁻ optical transitions are robust in linear-order to electric field and strain variations, resulting in
198 highly stable and homogeneous emission frequencies with lifetime-limited linewidths⁵³.

199 The S=1/2 electronic spin of SiV⁻ can be coherently controlled by either microwave or optical
200 driving, where the latter utilizes a GS-ES lambda (Λ) system tuned by an off-axis magnetic field.
201 However, coherent population trapping^{54,55} and Ramsey⁵⁶ experiments indicate a short spin
202 dephasing time $T_2^* \sim 100$ ns at 4 K. Phonon-mediated transitions between the two ground-state
203 orbital branches, separated by 50 GHz (≈ 2.5 K), represent the dominant contribution to spin
204 dephasing, arising from slightly different spin splitting in each orbital. Recently, by cooling SiV⁻ to
205 100 mK^{57,58}, spin coherence was extended to $T_2^* \approx 10$ μ s and $T_2 \approx 13$ ms for an isotopically-
206 purified sample⁵⁸, clearing the way for coherent manipulation of coupled nuclear memories.
207 Additionally, SiV⁻'s efficient ZPL emission, predominantly polarized into a single transition dipole,
208 makes it attractive for coupling to nanophotonic structures⁵⁹. Through precision placement of Si⁺
209 ions into a nanophotonic cavity, the entanglement signature between two emitters was observed⁶⁰
210 (Fig. 2c). Possessing similar spin and optical properties as SiV⁻, the germanium-vacancy (GeV⁻)
211 in diamond may offer stronger atom-light coupling due to its higher quantum efficiency^{61,62}.
212 Furthermore, the neutral charge state of SiV⁰^{63,64} and the tin-vacancy center^{65,66} have recently been
213 investigated to potentially combine a robust optical interface with long spin coherence at moderate
214 cryogenic temperatures, although optical spin readout for these systems has yet to be
215 demonstrated.

216 **Divacancy and Silicon-Vacancy in Silicon Carbide.** Silicon carbide (SiC) presents an
217 opportunity to integrate color centers into a technologically mature platform capable of wafer-
218 scale growth, fabrication, and doping⁶⁷. Unlike diamond, SiC exists in over 250 polytypes⁶⁸
219 (different stacking sequences of a silicon-carbon bilayer unit) to allow customizable material
220 properties and heterojunction devices, boosting the potential for interacting its hosted color center
221 spins with electrical or mechanical degrees of freedom^{69,70}. Among color centers investigated in
222 SiC, the divacancy and silicon vacancy defects have fulfilled key requirements for quantum
223 applications, including optical electron and nuclear spin addressability^{35,71}, long spin coherence⁷²⁻
224 ⁷⁴, and single defect isolation^{72,75}.

225 The neutral divacancy (V_C-V_{Si}; missing C atom next to missing Si atom) possesses the same C_{3v}
226 symmetry and number of active electrons as the NV center in diamond, leading to analogous spin

227 and optical structures⁶⁷ (Fig. 2d). Its spin-triplet GS exhibits electron coherence times T_2 that can
228 exceed 1 ms in samples with natural isotope abundance⁷². This extended coherence despite
229 higher fractions of nuclear spins than diamond stems from the larger lattice spacing in SiC and
230 the suppression of heteronuclear flip-flops between ²⁹Si and ¹³C at moderate magnetic fields ($T_2 >$
231 1 ms for $B > 15$ mT)^{76,77}. Crucially, divacancies have ZPLs at near-infrared wavelengths (~1100
232 nm) where significantly lower attenuation in optical fiber (~1 dB/km vs ~8 dB/km at 637 nm) will
233 facilitate entanglement generation over long distances. Recently, single divacancies, isolated in
234 the 4H and 3C polytypes, were shown to display well-resolved spin-dependent optical transitions
235 below 20 K, similar to the NV center (Fig. 2e)⁷⁸. Consequently, high-fidelity resonant readout⁷⁸ of
236 the divacancy spin (Fig. 2f) and Stark tuning of its optical transition frequencies⁷⁹ were
237 demonstrated at cryogenic temperatures, establishing critical elements for the implementation of
238 entanglement protocols¹¹. Harnessing the advantages of divacancies for long-range quantum
239 networks will also require improving their photon collection efficiency and natural ZPL emission
240 fraction (5-7%)⁷⁸. Towards this, 3C-SiC, which can be epitaxially grown as thin films on silicon,
241 presents an advanced platform for nanophotonic engineering^{80,81}.

242 The negatively charged silicon vacancy (V_{Si} ; single missing Si atom) diverges from the well-
243 studied NV-type level structure due to its odd number of active electrons that gives rise to a $S =$
244 $3/2$ ground-state and a complex set of optical transitions⁸². Notably, its spin properties and optical
245 readout at room temperature provide unique capabilities for thermometry⁸³ and vector
246 magnetometry⁸⁴. Single V_{Si} at both inequivalent lattice sites (V1 and V2 centers) in 4H-SiC have
247 been isolated, with both centers possessing coherence of order milliseconds under dynamical
248 decoupling^{73,74} and the V1 center emitting 40% of its photons into the ZPL at 4 K⁷⁴ (Fig. 2d,g). A
249 crucial step will be demonstration of the predicted excited state fine structure⁸² that enables
250 schemes for spin-photon entanglement.

251 **Rare-Earth Ions in Solids.** Due to shielding provided by their filled outer electronic shells, rare-
252 earth ions in solid-state crystals display $4f$ -electronic optical and spin levels with narrow intrinsic
253 linewidths and high spectral stability, reminiscent of free atoms. This isolation from environmental
254 noise has been exploited in rare-earth ensembles for photonic quantum memories, where the
255 quantum state of single photons are stored and retrieved via the collective optical and spin-wave
256 excitations of the ensemble^{3,85}. Moreover, rare earth impurities provide exceptionally long-lived
257 nuclear spins with relaxation and coherence times measured in units of days⁸⁶ and hours⁸⁷,
258 respectively. While these properties motivate rare-earth ensemble systems as leading platforms

259 for quantum repeaters and transducers^{88,89}, extending control to single rare-earth ions would
260 expand capabilities for programmable quantum circuits.

261 Recently, several groups have optically addressed single rare-earth ions, overcoming challenges
262 in signal-to-noise due to their weak optical emission and high background fluorescence in low
263 purity samples. These groups implemented techniques such as spectral isolation in micro-
264 crystallites^{90,91}, customized optics to minimize the confocal volume⁹², and fluorescence up-
265 conversion to levels with shorter optical lifetimes⁹³. Coherent control over single Ce³⁺ electron
266 spins in yttrium aluminum garnet (YAG) was demonstrated⁹⁴. Additionally, the hyperfine levels of
267 single Pr³⁺ ions in yttrium orthosilicate (YSO)^{90,91}, LaF₃⁹², and YAG⁹⁵ were spectroscopically
268 resolved, allowing nuclear spins to be initialized and read-out by resonant optical excitation and
269 manipulated by RF fields (Fig. 3a,b). Coherence of single nuclear spins in Pr:YAG was limited at
270 4 K by electron-phonon coupling⁹⁵ ($T_{1n} \sim 4 \mu\text{s}$), but can exceed seconds for Pr:YSO based on
271 ensemble measurements⁹⁶. Notably, an alternative detection route for single rare earths relies on
272 charge sensing of resonant photoionization, demonstrated for single Er³⁺ ions in a silicon single-
273 electron transistor (SET)⁹⁷.

274 The robustness of rare-earth systems to surface perturbations motivates nanophotonic
275 engineering as a promising route to ameliorate their low photon count rate. Recently, an atomic
276 frequency comb quantum memory with optical control over the storage time was demonstrated
277 for an small ensemble of Nd³⁺ ions in a nanophotonic cavity⁹⁸. Moreover, several groups reported
278 addressing single rare-earth ions exploiting cavity enhancement of their spontaneous emission
279 rate (Purcell factors >100)^{99,100}. Cavities can be fabricated directly into glassy rare-earth host
280 materials by focused ion beam milling^{98,99}. Additionally, they can be fabricated externally into a
281 material such as silicon and then transferred onto the rare-earth host for evanescent coupling¹⁰⁰.
282 These platforms set the stage for advances in optical control and remote entanglement of rare-
283 earth electrons and nuclei, as well as quantum routing of single photons, in integrated photonic
284 devices.

285 **Optically Active Donors in Silicon.** The miniaturization of silicon electronics to the nanoscale
286 has naturally broached the prospect for quantum systems in this technologically ubiquitous
287 platform. In recent years, the electron and nuclear spin of single ³¹P donors in silicon have been
288 read out by spin-dependent tunneling in an SET, demonstrating state-of-the-art coherence times
289 ($T_{2e} > 0.5 \text{ s}$ at 100 mK) and control fidelities (>99.99% for a single ³¹P nuclear spin)¹⁰¹. However,
290 coupling between multiple donor qubits in silicon remains an unsolved challenge, motivating

291 various proposals that span nanometer¹ to macroscopic length scales^{102,103}. Schemes requiring
292 strong coupling of individual donor spins to a common microwave resonator¹⁰² are difficult to
293 realize due to their small magnetic dipole moment. Recently, strong coupling between microwave
294 cavity photons and a single electron spin in a silicon double quantum dot was achieved only after
295 hybridizing the spin with its electronic wavefunction in the presence of an inhomogeneous
296 magnetic field^{104,105}. Alternatively, optical photon interconnects¹⁰³ could realize longer distance
297 couplings.

298 For group V shallow donors, optical transitions to excited orbital states occur in the far-infrared, a
299 technologically difficult regime. Instead, efforts have focused on transitions between the neutral
300 donor (D^0) and its donor-bound exciton (D^0X) with energies at 1.15 eV, near bandgap. In
301 isotopically-enriched ^{28}Si samples, these transitions are sufficiently narrow to resolve the
302 hyperfine structure of ^{31}P donors, allowing optical pumping through an Auger de-excitation to
303 hyperpolarize the electron and nuclear spin^{106,107}. This Auger decay occurs with near-unit
304 probability in indirect bandgap Si and enables electrical readout of long-lasting nuclear spin
305 coherence that exceeds 39 minutes at room temperature for ensembles of ionized donors^{106,107}.
306 However, the nonradiative nature of this process precludes optical detection or coupling of single
307 donors.

308 Recently, singly-ionized, chalcogen double donors (e.g., S^+ , Se^+) have begun to be investigated
309 for their stronger binding energies (~ 600 mV/ $2.9\ \mu\text{m}$) that permit donor optical transitions in the
310 mid-infrared (Fig. 3c)¹⁰³. Optical measurements on $^{77}\text{Se}^+$ ensembles at 1.2 K demonstrate
311 competitive electron spin coherence times ($T_{2,\text{Hahn}} = 2$ s for a qubit based on a clock transition)
312 and hyperfine-resolved optical transitions with narrow homogeneous linewidths (< 29 MHz).
313 Isolation of single chalcogen donors in the future could enable the use of silicon-on-insulator
314 photonics for cavity-enhanced readout and coupling¹⁰³.

315 **Applications of Quantum Registers and Memories**

316 In this section, we highlight recent advances that leverage the collective functionality of electron
317 and nuclear spins in solid-state defect systems for quantum applications.

318 **Quantum Networks.** Quantum networks that utilize shared entanglement between spatially
319 separated nodes represent the essential infrastructure for quantum key distribution and quantum
320 cloud computing, possessing security independent of the trustworthiness of the communicating
321 devices¹⁰⁸ or computing server¹⁰⁹. Although photons are ideal long-distance carriers of quantum

322 states, their conversion to long-lived stationary qubits is necessary for flexible timing of network
323 tasks and efficient propagation of entanglement over long distances⁴. These requirements are
324 fulfilled by the NV center in diamond, which combines a spin-light interface with control over local
325 nuclear memories. In 2013, a breakthrough experiment established entanglement between two
326 NV spins separated by three meters¹¹. Using the Barrett-Kok (BK) protocol, each NV center was
327 prepared to allow probabilistic emission of a photon correlated with its spin state. If the NV centers
328 emit indistinguishable photons (requiring the ZPL), overlapping their emitted modes on a beam-
329 splitter erases which-path information and causes detection of a single photon to project the NV
330 centers into an entangled state. Due to possible photon loss, detection of a second single photon
331 in an ensuing trial where both NV spins are flipped is required to confirm the entangled state,
332 leading to a low success probability $P_E \approx 10^{-7}$, proportional to the square of the photon collection
333 efficiency. Nevertheless, the high fidelity of the heralded entangled state ($\sim .92$), as well as its fast
334 tomography by single-shot readout, enabled the first loophole-free Bell test, using two NV centers
335 separated by 1.3 km¹¹⁰ (Fig. 4a,b).

336 Incorporating nuclear memories with remote electron entanglement empowers key network
337 primitives, such as teleportation, entanglement purification, and photonic quantum memory. The
338 state of the nitrogen nuclear spin associated with one NV center of an entangled pair was
339 unconditionally teleported (i.e., each attempt is successful) onto the electron spin of the other NV
340 center¹¹. Recently, entanglement purification, an essential capability of quantum repeaters that
341 “distills” a single high-fidelity entangled state from multiple lower fidelity copies, was achieved¹¹²
342 (Fig. 4c,d). Here, a low-quality entangled state is first generated between two NV spins by
343 detecting only a single output photon at the beam-splitter, forgoing the second trial of the BK
344 protocol^{11,110}. The entangled electron states are then swapped onto ¹³C nuclear spins at both
345 nodes, freeing the communication qubits for additional entanglement generation. Critically, the
346 weakly-coupled nuclear memories used are robust to several hundred optical cycles of the
347 electron³⁷, allowing the second entanglement generation to be attempted until success. The
348 memory qubits are finally projected onto a pure entangled state depending on the outcome of
349 local operations on the two entangled pairs¹¹². Since the purification protocol does not require
350 simultaneous detection of single photons in two consecutive entanglement attempts, it achieves
351 faster entanglement rates that scale linearly in photon detection probability.

352 While the above applications leverage the emission of spin-entangled photons, the NV's optical
353 interface additionally permits quantum storage of incident photons and absorption-based remote
354 entanglement¹¹³. Raman quantum memories for photons similar to those for rare-earth and atomic

355 systems were proposed for ensembles of NV centers^{114,115}, but have been difficult to realize due
356 to the crowded NV excited state structure and larger optical inhomogeneous broadening.
357 Alternatively, using a single NV center, photon polarization states were coherently transferred
358 onto the intrinsic nitrogen nuclear spin¹¹³ (Fig. 4e,f). This recent demonstration prepares the
359 electron and nitrogen nuclear spins in an entangled Bell state, and then utilizes the entangled
360 absorption of a photon in a degenerate optical Λ system¹¹⁶ to teleport the photon polarization onto
361 the nuclear spin. This approach paves the way for entanglement distribution between network
362 nodes through the absorption of entangled photon pairs at the NV resonant energy.

363 **Quantum Computing.** Overcoming the challenge of scaling a quantum computer to the large
364 number of qubits required to outperform classical algorithms hinges on correcting the inevitable
365 errors that arise due to the delicate, analogue nature of quantum states. While a potential
366 resolution lies in a monolithic architecture employing a large qubit array stabilized by topological
367 codes, a distributed or modular architecture that utilizes photonically linked nodes, each with only
368 a small number of qubits, could provide efficiencies due to its reconfigurable connections and
369 non-local quantum gates¹¹⁷. This distributed architecture is particularly applicable to defect-based
370 quantum registers of electron and nuclear spins, which satisfy the requirements for inter-node
371 photonic entanglement, as well as intra-node universal control and non-demolition readout.
372 Encouragingly, a distributed error correction approach using only four qubits per node was shown
373 to possess modest threshold error rates for the entangling links (~10%) and local operations
374 (~1%) that would allow a large-scale implementation to be fault-tolerant¹¹⁸.

375 Experimental efforts have so far focused on error correction within individual nodes. In 2014, two
376 groups^{30,40} demonstrated a majority-vote error correction protocol, encoding a quantum bit in a
377 logical qubit of three spins (Fig. 4g). These experiments leveraged advanced electron-nuclear
378 initialization sequences and quantum gates to correct a single bit-flip error automatically during
379 the decoding of the three-qubit register, avoiding direct measurement of error syndromes. More
380 recently, by utilizing non-demolition, single-shot readout at cryogenic temperatures, a stabilizer-
381 based approach¹¹⁹ involving active error detection and real-time feedback was implemented for a
382 logical qubit of three weakly-coupled ¹³C nuclei. This latter experiment demonstrated a
383 continuously phase-corrected logical qubit with coherence exceeding its best component qubit.
384 Future prospects include extending error correction to larger qubit registers and applying more
385 sophisticated codes to repair arbitrary single-qubit errors, or combining it with remote electron
386 entanglement for networked information processing. In addition, the potential to coherently
387 interface shallow NV centers with chemically-assembled nuclear spin arrays on the surface of

388 diamond could enable large-scale quantum simulations¹²⁰. Towards simulations of quantum
389 chemistry and condensed matter phases, proof-of-principle demonstrations with NV quantum
390 registers internal to diamond have deduced the energy structure of a HeH⁺ cation¹²¹ and a
391 topological wire coupled to a superconductor¹²².

392 **Quantum Sensing.** The atomic-scale dimensions, fast dynamics, and acute sensitivity of
393 quantum systems make them exceptional probes of their environment, combining high spatial
394 resolution, bandwidth, and precision. The challenge of quantum sensing is to isolate maximum
395 information about a target variable from its effect on the dynamics of the quantum sensor, which
396 simultaneously experiences decoherence and a multitude of competing influences⁶. The room-
397 temperature coherence of NV centers and its diverse deployment inside wide-field arrays¹²³,
398 nanoparticles¹²⁴, and scanning probes^{125–127} have precipitated their development as a
399 transformative technology for sensing magnetic fields and other external perturbations (Fig. 5a-
400 d). Wide-ranging efforts have leveraged the NV sensor for detection and characterization of
401 intracellular and biological processes^{123,124,128}, nanoscale nuclear magnetic resonance
402 (NMR)^{43,44,129,130}, magnetism in condensed matter systems^{125–127,131}, and device performance of
403 nanotechnologies^{132,133}.

404 In particular, NV detection of NMR spectroscopy significantly enhances the sensitivity and spatial
405 resolution of this powerful technique, promising chemical structure identification with single
406 molecule sensitivity and subcellular resolution (Fig. 5e,f). However, improving the frequency
407 resolution of NV detection to distinguish the few-hertz changes in NMR frequencies due to
408 chemical shifts and spin-spin couplings represents an ongoing pursuit. Pioneering works applied
409 DD sequences to single shallow NV centers to sense the magnetic field fluctuations from a
410 statistical polarization of $\sim 10^2$ external protons^{43,44}. These experiments demonstrated ~ 10 kHz
411 NMR linewidths, limited by T_2 of the NV sensor and diffusion of the target nuclei through the
412 nanoscale sensing volume. Correlation spectroscopy extends the phase acquisition time to the
413 electron T_1 (\sim ms), improving spectral resolution to several hundred hertz^{134,135}. Here, the phase
414 accumulated during an initial DD segment is stored in the polarization of the electron spin and
415 then correlated to the phase from a second DD segment after free evolution of the target nuclei.

416 Recently, the intrinsic nitrogen nuclear spin was leveraged as a longer-term memory for the initial
417 phase measured in correlation spectroscopy, extending the interrogation time to T_{1n} ($>$ minutes
418 for tesla-scale magnetic fields)^{136–138}. This approach naturally integrates repetitive, non-demolition
419 nuclear state readout^{31,130} and also frees the sensor electron spin so that its backaction on the

420 target nuclei, which shortens their correlation time, can be decoupled¹³⁷. Although sample
421 diffusion still limited the sensing duration (~5 ms), the nuclear memory approach resolved part-
422 per-million level chemical shifts in liquid state samples¹³⁹ (Fig. 5f). Alternatively, a recent NMR
423 scheme¹⁴⁰ utilized an NV ensemble and a synchronous readout technique^{141,142} that enables
424 frequency resolution independent of the sensor coherence time. Here, the larger sensing volume
425 mitigated the effects of diffusion and enabled access to the thermal, rather than statistical, nuclear
426 polarization, culminating in ~3 Hz spectral resolution to resolve chemical shifts and nuclear spin-
427 spin couplings¹⁴⁰.

428 **Challenges and Outlook**

429 Even with the enormous progress in impurity systems, the potential for improvement across the
430 spectrum of applications is limitless. Realizing kilohertz entanglement rates across metropolitan
431 distances, distributed logical qubits in a fault-tolerant network, or real-time intracellular NMR
432 spectroscopy, among other far-reaching goals, will require concerted advances in photonic and
433 device engineering, quantum control, and materials science. Moreover, while it may be enticing
434 to regard solid-state spins as a self-sufficient platform, exploration of their connection to diverse
435 quantum systems may lead to hybrid devices with optimized components. Recent advances in
436 interacting NV spins with microwave¹⁴³, acoustic^{144,145}, or magnonic excitations^{146,147} open new
437 routes toward on-chip state transfer and entanglement between impurity spins or hybrid systems.

438 While the solid-state environment poses challenges to impurity spins via phonon broadening and
439 total internal reflection of their emission, it also provides them their greatest asset, amenability to
440 fabrication and device integration. Coupling of optical emitters to photonic cavities with high
441 quality factors and small mode volumes concentrates their emission into the ZPL and into a single
442 cavity mode for efficient collection. A recent Fabry-Pérot microcavity design⁵⁰ directs 46% of the
443 NV center's emission into the ZPL, offering *in-situ* resonance tuning and reduced processing-
444 induced broadening of NV linewidths as advantages over previous monolithic diamond
445 approaches⁴⁶ (Fig. 6a). In parallel, novel defect platforms with robust ZPLs⁶⁰ or advanced
446 heteroepitaxy and selective etching techniques⁷⁸ will accelerate photonic cavity development (Fig.
447 6b). These advances will enable significantly higher rates of indistinguishable photons for long-
448 distance entanglement, as well as ultimately near-deterministic light-matter interactions in the
449 strong-coupling regime of cavity quantum electrodynamics. Towards continental-scale, fiber-
450 based quantum networks, defect systems with near-telecom wavelength emission, such as

451 divacancies in SiC or various rare earths, may offer additional avenues to create efficient
452 entanglement between solid-state nodes.

453 At a more local level, a promising direction lies in integrating impurity spins with on-chip photonics,
454 thereby creating field-deployable quantum sensors and compact information processing devices.
455 An integrated package using microfabricated photonic elements, including waveguides, couplers,
456 metalenses, and superconducting nanowire detectors, could crucially reduce optical losses and
457 eliminate bulky free-space optics^{48,148,149} (Fig. 6c). In these integrated photonic circuits, impurity
458 spins would provide powerful functionalities as single photon sources, photonic memories, and
459 nonlinear single-photon switches, establishing a scalable architecture for quantum processors
460 based on either photonic or modular matter-based qubits. Moreover, engineering of lab-on-a-chip
461 devices¹⁵⁰ and deployable probes, such as nanodiamonds attached directly to optical fibers¹⁵¹,
462 will proliferate the reach of quantum sensing. For example, diamond devices with surface-
463 structured microfluidic grooves realize both enhanced sensor-analyte contact for NMR
464 applications and increased photon collection efficiency by optical waveguiding¹⁵².

465 Advances in quantum control and materials science will naturally be fundamental to continued
466 progress. Encoding quantum memories in decoherence-free subspaces of two nuclear spins
467 would allow the use of more strongly-coupled nuclear spins while maintaining robustness to
468 optical excitation³⁷. This would increase speeds for interfacing quantum memories and enable
469 high-throughput, multiplexed versions of entanglement protocols, where entanglement is
470 continuously attempted using multiple memories before successes are heralded¹⁵³. Time-
471 dependent Hamiltonian engineering, such as optimal control¹⁵⁴ and shortcuts to adiabaticity¹⁵⁵,
472 could be extended for fast and robust gates despite densely spaced electron-nuclear energy
473 levels. Furthermore, the convergence of quantum error correction and quantum sensing could
474 improve sensitivity by extending qubit coherence regardless of the noise spectrum, in contrast to
475 dynamical decoupling. Pioneering demonstrations^{156,157} leveraged a single ancilla nuclear spin
476 that is robust against noise to correct the NV electron sensor. Finally, improvements in materials
477 engineering could overcome current limits to many applications, as well as open new
478 opportunities. Important challenges include the creation of high-density, near-surface defect
479 centers with long coherence times and a single orientation^{158–160}, control over defect charge states
480 by Fermi level tuning, and customized surface functionalization for targeted sensing tasks. In
481 addition, the discovery of novel impurity systems with superlative optical, spin, and host material
482 properties may aid in bringing solid-state spins closer to widely impactful quantum technologies.

483 **Acknowledgments**

484 We thank Alex Crook, F. J. Heremans, Paul Jerger, Kevin Miao, Tim Taminiau, Gary Wolfowicz,
485 and Tian Zhong for illuminating discussions. D.D.A. and B.B.Z. acknowledge support from the
486 National Science Foundation grant EFMA-164109, the Air Force Office of Scientific Research
487 grants FA9550-14-1-0231 and FA9550-15-1-0029, and the Army Research Office QSEP grant
488 W911NF-15-2-0058. R.H. acknowledges support from the Netherlands Organisation for Scientific
489 Research (NWO) through a VICI grant and the European Research Council (ERC) through a
490 Consolidator Grant. J.W. acknowledges support from ERC grant SMeL, the BW foundation,
491 BMBF grant BrainQSens, and the Max Planck Society.

492 **Correspondence and requests for materials should be addressed to D.D.A.**

493

494 **References**

- 495 1. Kane, B. E. A silicon-based nuclear spin quantum computer. *Nature* **393**, 133–137
496 (1998).
- 497 2. Hanson, R. & Awschalom, D. D. Coherent manipulation of single spins in
498 semiconductors. *Nature* **453**, 1043–1049 (2008).
- 499 3. de Riedmatten, H. & Afzelius, M. in *Engineering the Atom-Photon Interaction* (eds.
500 Predojević, A. & Mitchell, M. W.) 241–273 (Springer, 2015).
- 501 4. Munro, W. J., Azuma, K., Tamaki, K. & Nemoto, K. Inside Quantum Repeaters. *IEEE J.*
502 *Sel. Top. Quantum Electron.* **21**, 78–90 (2015).
- 503 5. Terhal, B. M. Quantum error correction for quantum memories. *Rev. Mod. Phys.* **87**, 307–
504 346 (2015).
- 505 6. Degen, C. L., Reinhard, F. & Cappellaro, P. Quantum sensing. *Rev. Mod. Phys.* **89**,
506 035002 (2017).
- 507 7. DiVincenzo, D. P. The Physical Implementation of Quantum Computation. *Fortschritte*
508 *Phys.* **48**, 771–783 (2000).
- 509 8. Doherty, M. W. *et al.* The nitrogen-vacancy colour centre in diamond. *Phys. Rep.* **528**, 1–
510 45 (2013).
- 511 9. Dutt, M. V. G. *et al.* Quantum Register Based on Individual Electronic and Nuclear Spin
512 Qubits in Diamond. *Science* **316**, 1312–1316 (2007).
- 513 10. Togan, E. *et al.* Quantum entanglement between an optical photon and a solid-state spin
514 qubit. *Nature* **466**, 730–736 (2010).
- 515 11. Bernien, H. *et al.* Heralded entanglement between solid-state qubits separated by three
516 metres. *Nature* **497**, 86–90 (2013).
- 517 12. Warburton, R. J. Single spins in self-assembled quantum dots. *Nat. Mater.* **12**, 483–493
518 (2013).
- 519 13. Lodahl, P. Quantum-dot based photonic quantum networks. *Quantum Sci. Technol.* **3**,
520 013001 (2018).
- 521 14. Vandersypen, L. M. K. *et al.* Interfacing spin qubits in quantum dots and donors—hot,
522 dense, and coherent. *npj Quantum Inf.* **3**, 34 (2017).
- 523 15. Aharonovich, I., Englund, D. & Toth, M. Solid-state single-photon emitters. *Nat. Photon.*
524 **10**, 631–641 (2016).
- 525 16. Shiue, R. J. *et al.* Active 2D materials for on-chip nanophotonics and quantum optics.
526 *Nanophotonics* **6**, 1329–1342 (2017).
- 527 17. Atatüre, M., Englund, D., Vamivakas, N., Lee, S.-Y. & Wrachtrup, J. Material platforms for
528 spin-based photonic quantum technologies. *Nat. Rev. Mater.* **3**, 38–51 (2018).
- 529 18. Robledo, L. *et al.* High-fidelity projective read-out of a solid-state spin quantum register.

- 530 *Nature* **477**, 574–578 (2011).
- 531 19. Childress, L. *et al.* Coherent Dynamics of Coupled Electron and Nuclear Spin Qubits in
532 Diamond. *Science* **314**, 281–285 (2006).
- 533 20. Humphreys, P. C. *et al.* Deterministic delivery of remote entanglement on a quantum
534 network. *Nature* **558**, 268–273 (2018).
- 535 21. Jarmola, A., Acosta, V. M., Jensen, K., Chemerisov, S. & Budker, D. Temperature- and
536 Magnetic-Field-Dependent Longitudinal Spin Relaxation in Nitrogen-Vacancy Ensembles
537 in Diamond. *Phys. Rev. Lett.* **108**, 197601 (2012).
- 538 22. Astner, T. *et al.* Solid-state electron spin lifetime limited by phononic vacuum modes. *Nat.*
539 *Mater.* **17**, 313–317 (2018).
- 540 23. Zhao, N. *et al.* Sensing single remote nuclear spins. *Nat. Nanotech.* **7**, 657–662 (2012).
- 541 24. Balasubramanian, G. *et al.* Ultralong spin coherence time in isotopically engineered
542 diamond. *Nat. Mater.* **8**, 383–387 (2009).
- 543 25. Bar-Gill, N., Pham, L. M., Jarmola, A., Budker, D. & Walsworth, R. L. Solid-state
544 electronic spin coherence time approaching one second. *Nat. Commun.* **4**, 1743 (2012).
- 545 26. Neumann, P. *et al.* Multipartite entanglement among single spins in diamond. *Science*
546 **320**, 1326–1329 (2008).
- 547 27. Fuchs, G. D., Burkard, G., Klimov, P. V. & Awschalom, D. D. A quantum memory intrinsic
548 to single nitrogen–vacancy centres in diamond. *Nat. Phys.* **7**, 789–793 (2011).
- 549 28. Dréau, A., Maze, J. R., Lesik, M., Roch, J. F. & Jacques, V. High-resolution spectroscopy
550 of single NV defects coupled with nearby ¹³C nuclear spins in diamond. *Phys. Rev. B* **85**,
551 134107 (2012).
- 552 29. Jelezko, F. *et al.* Observation of Coherent Oscillation of a Single Nuclear Spin and
553 Realization of a Two-Qubit Conditional Quantum Gate. *Phys. Rev. Lett.* **93**, 130501
554 (2004).
- 555 30. Waldherr, G. *et al.* Quantum error correction in a solid-state hybrid spin register. *Nature*
556 **506**, 204–207 (2014).
- 557 31. Neumann, P. *et al.* Single-Shot Readout of a Single Nuclear Spin. *Science* **329**, 542–544
558 (2010).
- 559 32. Maurer, P. C. *et al.* Room-Temperature Quantum Bit Memory Exceeding One Second.
560 *Science* **336**, 1283–1286 (2012).
- 561 33. Pfender, M. *et al.* Protecting a Diamond Quantum Memory by Charge State Control.
562 *Nano Lett.* **17**, 5931–5937 (2017).
- 563 34. Jacques, V. *et al.* Dynamic Polarization of Single Nuclear Spins by Optical Pumping of
564 Nitrogen-Vacancy Color Centers in Diamond at Room Temperature. *Phys. Rev. Lett.* **102**,
565 057403 (2009).
- 566 35. Falk, A. L. *et al.* Optical Polarization of Nuclear Spins in Silicon Carbide. *Phys. Rev. Lett.*

- 567 **114**, 247603 (2015).
- 568 36. Ivády, V. *et al.* Theoretical model of dynamic spin polarization of nuclei coupled to
569 paramagnetic point defects in diamond and silicon carbide. *Phys. Rev. B* **92**, 115206
570 (2015).
- 571 37. Reiserer, A. *et al.* Robust Quantum-Network Memory Using Decoherence-Protected
572 Subspaces of Nuclear Spins. *Phys. Rev. X* **6**, 021040 (2016).
- 573 38. Kolkowitz, S., Unterreithmeier, Q. P., Bennett, S. D. & Lukin, M. D. Sensing Distant
574 Nuclear Spins with a Single Electron Spin. *Phys. Rev. Lett.* **109**, 137601 (2012).
- 575 39. Taminiau, T. H. *et al.* Detection and control of individual nuclear spins using a weakly
576 coupled electron spin. *Phys. Rev. Lett.* **109**, 137602 (2012).
- 577 40. Taminiau, T. H., Cramer, J., van der Sar, T., Dobrovitski, V. V & Hanson, R. Universal
578 control and error correction in multi-qubit spin registers in diamond. *Nat. Nanotech.* **9**,
579 171–176 (2014).
- 580 41. Liu, G.-Q. *et al.* Single-Shot Readout of a Nuclear Spin Weakly Coupled to a Nitrogen-
581 Vacancy Center at Room Temperature. *Phys. Rev. Lett.* **118**, 150504 (2017).
- 582 42. Dolde, F. *et al.* Room-temperature entanglement between single defect spins in diamond.
583 *Nat. Phys.* **9**, 139–143 (2013).
- 584 43. Staudacher, T. *et al.* Nuclear magnetic resonance spectroscopy on a (5-nanometer)³
585 sample volume. *Science* **339**, 561–563 (2013).
- 586 44. Mamin, H. J. *et al.* Nanoscale Nuclear Magnetic Resonance with a Nitrogen-Vacancy
587 Spin Sensor. *Science* **339**, 557–560 (2013).
- 588 45. Barclay, P. E., Fu, K.-M. C., Santori, C., Faraon, A. & Beausoleil, R. G. Hybrid Nanocavity
589 Resonant Enhancement of Color Center Emission in Diamond. *Phys. Rev. X* **1**, 011007
590 (2011).
- 591 46. Faraon, A., Santori, C., Huang, Z., Acosta, V. M. & Beausoleil, R. G. Coupling of
592 Nitrogen-Vacancy Centers to Photonic Crystal Cavities in Monocrystalline Diamond.
593 *Phys. Rev. Lett.* **109**, 033604 (2012).
- 594 47. Aharonovich, I. & Neu, E. Diamond nanophotonics. *Adv. Opt. Mater.* **2**, 911–928 (2014).
- 595 48. Schröder, T. *et al.* Quantum nanophotonics in diamond. *J. Opt. Soc. Am. B* **33**, B65–B83
596 (2016).
- 597 49. Zaske, S. *et al.* Visible-to-Telecom Quantum Frequency Conversion of Light from a
598 Single Quantum Emitter. *Phys. Rev. Lett.* **109**, 147404 (2012).
- 599 50. Riedel, D. *et al.* Deterministic Enhancement of Coherent Photon Generation from a
600 Nitrogen-Vacancy Center in Ultrapure Diamond. *Phys. Rev. X* **7**, 031040 (2017).
- 601 51. Dréau, A., Tchekorotova, A., Mahdaoui, A. El, Bonato, C. & Hanson, R. Quantum
602 frequency conversion to telecom of single photons from a nitrogen-vacancy center in
603 diamond. Preprint at <http://arxiv.org/abs/1801.03304> (2018).

- 604 52. Hepp, C. *et al.* Electronic Structure of the Silicon Vacancy Color Center in Diamond.
605 *Phys. Rev. Lett.* **112**, 036405 (2014).
- 606 53. Rogers, L. J. *et al.* Multiple intrinsically identical single-photon emitters in the solid state.
607 *Nat. Commun.* **5**, 4739 (2014).
- 608 54. Pingault, B. *et al.* All-Optical Formation of Coherent Dark States of Silicon-Vacancy Spins
609 in Diamond. *Phys. Rev. Lett.* **113**, 263601 (2014).
- 610 55. Rogers, L. J. *et al.* All-Optical Initialization, Readout, and Coherent Preparation of Single
611 Silicon-Vacancy Spins in Diamond. *Phys. Rev. Lett.* **113**, 263602 (2014).
- 612 56. Pingault, B. *et al.* Coherent control of the silicon-vacancy spin in diamond. *Nat. Commun.*
613 **8**, 15579 (2017).
- 614 57. Becker, J. N. *et al.* All-Optical Control of the Silicon-Vacancy Spin in Diamond at
615 Millikelvin Temperatures. *Phys. Rev. Lett.* **120**, 053603 (2018).
- 616 58. Sukachev, D. D. *et al.* Silicon-Vacancy Spin Qubit in Diamond: A Quantum Memory
617 Exceeding 10 ms with Single-Shot State Readout. *Phys. Rev. Lett.* **119**, 223602 (2017).
- 618 59. Rogers, L. J. *et al.* Electronic structure of the negatively charged silicon-vacancy center in
619 diamond. *Phys. Rev. B* **89**, 235101 (2014).
- 620 60. Sipahigil, A. *et al.* An integrated diamond nanophotonics platform for quantum-optical
621 networks. *Science* **354**, 847–850 (2016).
- 622 61. Bhaskar, M. K. *et al.* Quantum Nonlinear Optics with a Germanium-Vacancy Color Center
623 in a Nanoscale Diamond Waveguide. *Phys. Rev. Lett.* **118**, 223603 (2017).
- 624 62. Siyushev, P. *et al.* Optical and microwave control of germanium-vacancy center spins in
625 diamond. *Phys. Rev. B* **96**, 081201 (2017).
- 626 63. Green, B. L. *et al.* Neutral Silicon-Vacancy Center in Diamond: Spin Polarization and
627 Lifetimes. *Phys. Rev. Lett.* **119**, 096402 (2017).
- 628 64. Rose, B. C. *et al.* Observation of an environmentally insensitive solid state spin defect in
629 diamond. Preprint at <https://arxiv.org/abs/1706.01555> (2017).
- 630 65. Tchernij, S. D. *et al.* Single-Photon-Emitting Optical Centers in Diamond Fabricated upon
631 Sn Implantation. *ACS Photonics* **4**, 2580–2586 (2017).
- 632 66. Iwasaki, T. *et al.* Tin-Vacancy Quantum Emitters in Diamond. *Phys. Rev. Lett.* **119**,
633 253601 (2017).
- 634 67. Koehl, W. F., Buckley, B. B., Heremans, F. J., Calusine, G. & Awschalom, D. D. Room
635 temperature coherent control of defect spin qubits in silicon carbide. *Nature* **479**, 84–87
636 (2011).
- 637 68. Falk, A. L. *et al.* Polytype control of spin qubits in silicon carbide. *Nat. Commun.* **4**, 1819
638 (2013).
- 639 69. Falk, A. L. *et al.* Electrically and Mechanically Tunable Electron Spins in Silicon Carbide
640 Color Centers. *Phys. Rev. Lett.* **112**, 187601 (2014).

- 641 70. Whiteley, S. J. *et al.* Coherent Control of Spins with Gaussian Acoustics. Preprint at
642 <https://arxiv.org/abs/1804.10996> (2018).
- 643 71. Klimov, P. V, Falk, A. L., Christle, D. J., Dobrovitski, V. V & Awschalom, D. D. Quantum
644 entanglement at ambient conditions in a macroscopic solid-state spin ensemble. *Sci. Adv.*
645 **1**, e1501015 (2015).
- 646 72. Christle, D. J. *et al.* Isolated electron spins in silicon carbide with millisecond coherence
647 times. *Nat. Mater.* **14**, 160–163 (2014).
- 648 73. Simin, D. *et al.* Locking of electron spin coherence above 20 ms in natural silicon carbide.
649 *Phys. Rev. B* **95**, 161201 (2017).
- 650 74. Nagy, R. *et al.* Quantum Properties of Dichroic Silicon Vacancies in Silicon Carbide.
651 *Phys. Rev. Appl.* **9**, 034022 (2018).
- 652 75. Widmann, M. *et al.* Coherent control of single spins in silicon carbide at room
653 temperature. *Nat. Mater.* **14**, 164–168 (2014).
- 654 76. Yang, L.-P. *et al.* Electron spin decoherence in silicon carbide nuclear spin bath. *Phys.*
655 *Rev. B* **90**, 241203 (2014).
- 656 77. Seo, H. *et al.* Quantum decoherence dynamics of divacancy spins in silicon carbide. *Nat.*
657 *Commun.* **7**, 12935 (2016).
- 658 78. Christle, D. J. *et al.* Isolated Spin Qubits in SiC with a High-Fidelity Infrared Spin-to-
659 Photon Interface. *Phys. Rev. X* **7**, 021046 (2017).
- 660 79. de las Casas, C. F. *et al.* Stark tuning and electrical charge state control of single
661 divacancies in silicon carbide. *Appl. Phys. Lett.* **111**, 262403 (2017).
- 662 80. Radulaski, M. *et al.* Photonic crystal cavities in cubic (3C) polytype silicon carbide films.
663 *Opt. Express* **21**, 32623–32629 (2013).
- 664 81. Calusine, G., Politi, A. & Awschalom, D. D. Cavity-Enhanced Measurements of Defect
665 Spins in Silicon Carbide. *Phys. Rev. Appl.* **6**, 014019 (2016).
- 666 82. Soykal, O., Dev, P. & Economou, S. E. Silicon vacancy center in 4H -SiC: Electronic
667 structure and spin-photon interfaces. *Phys. Rev. B* **93**, 081207(R) (2016).
- 668 83. Kraus, H. *et al.* Magnetic field and temperature sensing with atomic-scale spin defects in
669 silicon carbide. *Sci. Rep.* **4**, 5303 (2014).
- 670 84. Niethammer, M. *et al.* Vector Magnetometry Using Silicon Vacancies in 4H-SiC Under
671 Ambient Conditions. *Phys. Rev. Appl.* **6**, 034001 (2016).
- 672 85. Heshami, K. *et al.* Quantum memories: emerging applications and recent advances. *J.*
673 *Mod. Opt.* **63**, 2005–2028 (2016).
- 674 86. Könz, F. *et al.* Temperature and concentration dependence of optical dephasing,
675 spectral-hole lifetime, and anisotropic absorption in Eu³⁺:Y₂SiO₅. *Phys. Rev. B* **68**,
676 085109 (2003).
- 677 87. Zhong, M. *et al.* Optically addressable nuclear spins in a solid with a six-hour coherence

- 678 time. *Nature* **517**, 177–180 (2015).
- 679 88. O'Brien, C., Lauk, N., Blum, S., Morigi, G. & Fleischhauer, M. Interfacing
680 Superconducting Qubits and Telecom Photons via a Rare-Earth-Doped Crystal. *Phys.*
681 *Rev. Lett.* **113**, 063603 (2014).
- 682 89. Williamson, L. A., Chen, Y.-H. & Longdell, J. J. Magneto-Optic Modulator with Unit
683 Quantum Efficiency. *Phys. Rev. Lett.* **113**, 203601 (2014).
- 684 90. Utikal, T. *et al.* Spectroscopic detection and state preparation of a single praseodymium
685 ion in a crystal. *Nat. Commun.* **5**, 3627 (2014).
- 686 91. Eichhammer, E., Utikal, T., Götzinger, S. & Sandoghdar, V. Spectroscopic detection of
687 single Pr³⁺ ions on the ³H₄ – ¹D₂ transition. *New J. Phys.* **17**, 083018 (2015).
- 688 92. Nakamura, I., Yoshihiro, T., Inagawa, H., Fujiyoshi, S. & Matsushita, M. Spectroscopy of
689 single Pr³⁺ ion in LaF₃ crystal at 1.5 K. *Sci. Rep.* **4**, 7364 (2015).
- 690 93. Kolesov, R. *et al.* Optical detection of a single rare-earth ion in a crystal. *Nat. Commun.* **3**,
691 1029 (2012).
- 692 94. Siyushev, P. *et al.* Coherent properties of single rare-earth spin qubits. *Nat. Commun.* **5**,
693 3895 (2014).
- 694 95. Xia, K. *et al.* Optical and spin properties of a single praseodymium ion in a crystal.
695 Preprint at <http://arxiv.org/abs/1706.08736> (2017).
- 696 96. Fraval, E., Sellars, M. J. & Longdell, J. J. Dynamic Decoherence Control of a Solid-State
697 Nuclear-Quadrupole Qubit. *Phys. Rev. Lett.* **95**, 030506 (2005).
- 698 97. Yin, C. *et al.* Optical addressing of an individual erbium ion in silicon. *Nature* **497**, 91–94
699 (2013).
- 700 98. Zhong, T. *et al.* Nanophotonic rare-earth quantum memory with optically controlled
701 retrieval. *Science* **357**, 1392–1395 (2017).
- 702 99. Zhong, T. *et al.* Optically addressing single rare-earth ions in a nanophotonic cavity.
703 Preprint at <http://arxiv.org/abs/1803.07520> (2018).
- 704 100. Dibos, A., Raha, M., Phenicie, C. & Thompson, J. Isolating and enhancing the emission
705 of single erbium ions using a silicon nanophotonic cavity. Preprint at
706 <http://arxiv.org/abs/1711.10368> (2017).
- 707 101. Muhonen, J. T. *et al.* Storing quantum information for 30 seconds in a nanoelectronic
708 device. *Nat. Nanotech.* **9**, 986–991 (2014).
- 709 102. Tosi, G., Mohiyaddin, F. A., Huebl, H. & Morello, A. Circuit-quantum electrodynamics with
710 direct magnetic coupling to single-atom spin qubits in isotopically enriched ²⁸Si. *AIP*
711 *Adv.* **4**, 087122 (2014).
- 712 103. Morse, K. J. *et al.* A photonic platform for donor spin qubits in silicon. *Sci. Adv.* **3**,
713 e1700930 (2017).
- 714 104. Mi, X. *et al.* A coherent spin–photon interface in silicon. *Nature* **555**, 599–603 (2018).

- 715 105. Samkharadze, N. *et al.* Strong spin-photon coupling in silicon. *Science* **359**, 1123–1127
716 (2018).
- 717 106. Steger, M. *et al.* Quantum Information Storage for over 180 s Using Donor Spins in a
718 ²⁸Si ‘Semiconductor Vacuum’. *Science* **336**, 1280–1283 (2012).
- 719 107. Saeedi, K. *et al.* Room-Temperature Quantum Bit Storage Exceeding 39 Minutes Using
720 Ionized Donors in Silicon-28. *Science* **342**, 830–833 (2013).
- 721 108. Vazirani, U. & Vidick, T. Fully Device-Independent Quantum Key Distribution. *Phys. Rev.*
722 *Lett.* **113**, 140501 (2014).
- 723 109. Barz, S. *et al.* Demonstration of Blind Quantum Computing. *Science* **335**, 303–308
724 (2012).
- 725 110. Hensen, B. *et al.* Loophole-free Bell inequality violation using electron spins separated by
726 1.3 kilometres. *Nature* **526**, 682–686 (2015).
- 727 111. Pfaff, W. *et al.* Unconditional quantum teleportation between distant solid-state quantum
728 bits. *Science* **345**, 532–535 (2014).
- 729 112. Kalb, N. *et al.* Entanglement distillation between solid-state quantum network nodes.
730 *Science* **356**, 928–932 (2017).
- 731 113. Yang, S. *et al.* High-fidelity transfer and storage of photon states in a single nuclear spin.
732 *Nat. Photon.* **10**, 507–511 (2016).
- 733 114. Heshami, K. *et al.* Raman quantum memory based on an ensemble of nitrogen-vacancy
734 centers coupled to a microcavity. *Phys. Rev. A* **89**, 040301 (2014).
- 735 115. Poem, E. *et al.* Broadband noise-free optical quantum memory with neutral nitrogen-
736 vacancy centers in diamond. *Phys. Rev. B* **91**, 205108 (2015).
- 737 116. Kosaka, H. & Niikura, N. Entangled Absorption of a Single Photon with a Single Spin in
738 Diamond. *Phys. Rev. Lett.* **114**, 053603 (2015).
- 739 117. Monroe, C. *et al.* Large-scale modular quantum-computer architecture with atomic
740 memory and photonic interconnects. *Phys. Rev. A* **89**, 022317 (2014).
- 741 118. Nickerson, N. H., Li, Y. & Benjamin, S. C. Topological quantum computing with a very
742 noisy network and local error rates approaching one percent. *Nat. Commun.* **4**, 1756
743 (2013).
- 744 119. Cramer, J. *et al.* Repeated quantum error correction on a continuously encoded qubit by
745 real-time feedback. *Nat. Commun.* **7**, 11526 (2016).
- 746 120. Cai, J., Retzker, A., Jelezko, F. & Plenio, M. B. A large-scale quantum simulator on a
747 diamond surface at room temperature. *Nat. Phys.* **9**, 168–173 (2013).
- 748 121. Wang, Y. *et al.* Quantum Simulation of Helium Hydride Cation in a Solid-State Spin
749 Register. *ACS Nano* **9**, 7769–7774 (2015).
- 750 122. Kong, F. *et al.* Direct Measurement of Topological Numbers with Spins in Diamond. *Phys.*
751 *Rev. Lett.* **117**, 060503 (2016).

- 752 123. Le Sage, D. *et al.* Optical magnetic imaging of living cells. *Nature* **496**, 486–489 (2013).
- 753 124. Simpson, D. A. *et al.* Non-Neurotoxic Nanodiamond Probes for Intraneuronal
754 Temperature Mapping. *ACS Nano* **11**, 12077–12086 (2017).
- 755 125. Thiel, L. *et al.* Quantitative nanoscale vortex imaging using a cryogenic quantum
756 magnetometer. *Nat. Nanotech.* **11**, 677–681 (2016).
- 757 126. Pelliccione, M. *et al.* Scanned probe imaging of nanoscale magnetism at cryogenic
758 temperatures with a single-spin quantum sensor. *Nat. Nanotech.* **11**, 700–705 (2016).
- 759 127. Gross, I. *et al.* Real-space imaging of non-collinear antiferromagnetic order with a single-
760 spin magnetometer. *Nature* **549**, 252–256 (2017).
- 761 128. Barry, J. F. *et al.* Optical magnetic detection of single-neuron action potentials using
762 quantum defects in diamond. *Proc. Natl. Acad. Sci.* **113**, 14133–14138 (2016).
- 763 129. Shi, F. *et al.* Single-protein spin resonance spectroscopy under ambient conditions.
764 *Science* **347**, 1135–1138 (2015).
- 765 130. Lovchinsky, I. *et al.* Nuclear magnetic resonance detection and spectroscopy of single
766 proteins using quantum logic. *Science* **351**, 836–841 (2016).
- 767 131. Casola, F., van der Sar, T. & Yacoby, A. Probing condensed matter physics with
768 magnetometry based on nitrogen-vacancy centres in diamond. *Nat. Rev. Mater.* **3**, 17088
769 (2018).
- 770 132. Appel, P., Ganzhorn, M., Neu, E. & Maletinsky, P. Nanoscale microwave imaging with a
771 single electron spin in diamond. *New J. Phys.* **17**, 112001 (2015).
- 772 133. Jakobi, I. *et al.* Measuring broadband magnetic fields on the nanoscale using a hybrid
773 quantum register. *Nat. Nanotech.* **12**, 67–72 (2016).
- 774 134. Laraoui, A. *et al.* High-resolution correlation spectroscopy of ¹(³)C spins near a
775 nitrogen-vacancy centre in diamond. *Nat. Commun.* **4**, 1651 (2013).
- 776 135. Kong, X., Stark, A., Du, J., McGuinness, L. P. & Jelezko, F. Towards Chemical Structure
777 Resolution with Nanoscale Nuclear Magnetic Resonance Spectroscopy. *Phys. Rev. Appl.*
778 **4**, 024004 (2015).
- 779 136. Zaiser, S. *et al.* Enhancing quantum sensing sensitivity by a quantum memory. *Nat.*
780 *Commun.* **7**, 12279 (2016).
- 781 137. Pfender, M. *et al.* Nonvolatile nuclear spin memory enables sensor-unlimited nanoscale
782 spectroscopy of small spin clusters. *Nat. Commun.* **8**, 834 (2017).
- 783 138. Roskopf, T., Zopes, J., Boss, J. M. & Degen, C. L. A quantum spectrum analyzer
784 enhanced by a nuclear spin memory. *npj Quantum Inf.* **3**, 33 (2017).
- 785 139. Aslam, N. *et al.* Nanoscale nuclear magnetic resonance with chemical resolution. *Science*
786 **357**, 67–71 (2017).
- 787 140. Glenn, D. R. *et al.* High-resolution magnetic resonance spectroscopy using a solid-state
788 spin sensor. *Nature* **555**, 351–354 (2018).

- 789 141. Boss, J. M., Cujia, K. S., Zopes, J. & Degen, C. L. Quantum sensing with arbitrary
790 frequency resolution. *Science* **356**, 837–840 (2017).
- 791 142. Schmitt, S. *et al.* Submillihertz magnetic spectroscopy performed with a nanoscale
792 quantum sensor. *Science* **356**, 832–837 (2017).
- 793 143. Astner, T. *et al.* Coherent Coupling of Remote Spin Ensembles via a Cavity Bus. *Phys.*
794 *Rev. Lett.* **118**, 140502 (2017).
- 795 144. Barfuss, A., Teissier, J., Neu, E., Nunnenkamp, A. & Maletinsky, P. Strong mechanical
796 driving of a single electron spin. *Nat. Phys.* **11**, 820–824 (2015).
- 797 145. Lee, D., Lee, K. W., Cady, J. V., Ovartchaiyapong, P. & Jayich, A. C. B. Topical review:
798 spins and mechanics in diamond. *J. Opt.* **19**, 033001 (2017).
- 799 146. Wolfe, C. S. *et al.* Off-resonant manipulation of spins in diamond via precessing
800 magnetization of a proximal ferromagnet. *Phys. Rev. B* **89**, 180406 (2014).
- 801 147. Andrich, P. *et al.* Long-range spin wave mediated control of defect qubits in
802 nanodiamonds. *npj Quantum Inf.* **3**, 28 (2017).
- 803 148. Najafi, F. *et al.* On-chip detection of non-classical light by scalable integration of single-
804 photon detectors. *Nat. Commun.* **6**, 5873 (2015).
- 805 149. Grote, R. R. *et al.* Imaging a Nitrogen-Vacancy Center with a Diamond Immersion
806 Metalens.
- 807 Preprint at <http://arxiv.org/abs/1711.00901> (2017).
- 808 150. Steinert, S. *et al.* Magnetic spin imaging under ambient conditions with sub-cellular
809 resolution. *Nat. Commun.* **4**, (2013).
- 810 151. Fedotov, I. V. *et al.* Electron spin manipulation and readout through an optical fiber. *Sci.*
811 *Rep.* **4**, 5362 (2015).
- 812 152. Kehayias, P. *et al.* Solution nuclear magnetic resonance spectroscopy on a
813 nanostructured diamond chip. *Nat. Commun.* **8**, 188 (2017).
- 814 153. van Dam, S. B., Humphreys, P. C., Rozpędek, F., Wehner, S. & Hanson, R. Multiplexed
815 entanglement generation over quantum networks using multi-qubit nodes. *Quantum Sci.*
816 *Technol.* **2**, 034002 (2017).
- 817 154. Geng, J. *et al.* Experimental Time-Optimal Universal Control of Spin Qubits in Solids.
818 *Phys. Rev. Lett.* **117**, 170501 (2016).
- 819 155. Zhou, B. B. *et al.* Accelerated quantum control using superadiabatic dynamics in a solid-
820 state lambda system. *Nat. Phys.* **13**, 330–334 (2017).
- 821 156. Hirose, M. & Cappellaro, P. Coherent feedback control of a single qubit in diamond.
822 *Nature* **532**, 77–80 (2016).
- 823 157. Unden, T. *et al.* Quantum Metrology Enhanced by Repetitive Quantum Error Correction.
824 *Phys. Rev. Lett.* **116**, 230502 (2016).

- 825 158. Lesik, M. *et al.* Perfect preferential orientation of nitrogen-vacancy defects in a synthetic
826 diamond sample. *Appl. Phys. Lett.* **104**, 113107 (2014).
- 827 159. Michl, J. *et al.* Perfect alignment and preferential orientation of nitrogen-vacancy centers
828 during chemical vapor deposition diamond growth on (111) surfaces. *Appl. Phys. Lett.*
829 **104**, 102407 (2014).
- 830 160. Fukui, T. *et al.* Perfect selective alignment of nitrogen-vacancy centers in diamond. *Appl.*
831 *Phys. Express* **7**, 055201 (2014).
- 832

833 **Figure 1 | The NV center in diamond and nearby nuclear spins.**

834 **a)** Schematic of an NV⁻ center in diamond. The NV electron spin is coupled to proximal nuclear
835 spins, such as its intrinsic ¹⁴N and lattice ¹³C. **b)** PL into the phonon sideband (PSB) as the
836 detuning of a laser is scanned across the NV center ZPL (637.2 nm, $T = 7$ K). Resonant transitions
837 to six spin-orbit excited states follow spin-selection rules and enable optical spin initialization,
838 readout, and entanglement. Cycling transitions are labeled in green, while non-cycling transitions
839 are labeled in orange. **c)** Coherence time T_2 of an NV center ensemble in isotopically-purified
840 diamond (0.01% ¹³C) as a function of the number of pulses n in a dynamical decoupling sequence,
841 for various temperatures. **d)** Optically detected magnetic resonance (ODMR) spectrum taken by
842 sweeping the frequency of a microwave field and measuring the NV center PL. The NV electronic
843 transition $|m_s = 0\rangle$ to $| - 1\rangle$ is split due to interaction with three strongly-coupled nuclear spins
844 (hyperfine couplings: ¹⁴N, 2.16 MHz; ¹³C₁, 413 kHz; ¹³C₂, 89 kHz). **e)** (left) Single-shot readout
845 protocol for strongly-coupled nuclear spins. The following block is repeated: the nuclear spin state
846 (here for ¹³C₁) is correlated to the electron spin state by a controlled-not operation and then the
847 electron state is read out. (right) Fluorescence time trace showing quantum jumps between
848 nuclear spin states. **f)** Illustration of hyperfine coupling. If the electron spin is in $|m_s = 0\rangle$, the
849 nuclear spin precesses with frequency ω_0 about the applied magnetic field \vec{B} , while in $|m_s = -1\rangle$,
850 the nuclear precession frequency ω_{-1} and axis are modified by the hyperfine components A_{\parallel} and
851 A_{\perp} , which depend on relative position between the nuclear and electron spin. **g)** Schematic for
852 the evolution of a nuclear spin when the electron spin is repeatedly flipped by a dynamical
853 decoupling sequence. When the spacing between the electronic π -pulses is in resonance with a
854 half-period of the nuclear Larmor precession, the nuclear spin effectively rotates in opposite
855 directions depending on the initial electron spin state. **h)** Data showing conditional control over a
856 weakly-coupled nuclear spin by a dynamical decoupling sequence. The electron spin state
857 determines the nuclear rotation direction, while the number of pulses N determines the total
858 rotation angle.

859 Figures reproduced from: a) Ref. ²³; b) Ref. ¹⁰; c) Ref. ²⁵; d) e) Ref. ³⁰; f) Ref. ³⁷; g) Ref. ³⁸; h) Ref.
860 ⁴⁰.

861

862 **Figure 2 | The silicon vacancy center in diamond and color centers in silicon carbide.**

863 **a)** Orbital structure of the SiV^- center, showing doublets in both the ground and excited state that
864 are split by spin-orbit coupling. **b)** PL spectrum of the SiV^- center in diamond, displaying four zero-
865 phonon lines corresponding to transitions labeled in a) (linewidths shown are limited by
866 spectrometer resolution). The SiV^- center's high Debye-Waller factor (~70% of total emission into
867 ZPLs at 4 K), lifetime-limited optical linewidths, and robustness to spectral diffusion make it an
868 attractive source for indistinguishable photons. **c)** Scanning electron micrograph (SEM) of
869 diamond nanophotonic cavities with SiV^- centers incorporated by precision ion implantation
870 (upper). The orbital states of two SiV^- centers can be entangled by the emission of a single
871 indistinguishable Raman photon into a nanophotonic waveguide (lower). This entangled state is
872 observed by its enhanced photon scattering statistics. **d)** Structure of 4H-SiC, showing two non-
873 equivalent atomic sites for the Si and C atoms (h – quasihexagonal, k – quasicubic). There are
874 two inequivalent forms of the silicon vacancy (V_{Si}) and four inequivalent forms of the divacancy
875 ($V_{\text{C}}-V_{\text{Si}}$) in 4H-SiC. **e)** PL excitation measurement by scanning the detuning of a laser about the
876 ZPL of a single divacancy (hh) in 4H-SiC (1132 nm, $T = 8$ K). The excited state fine structure and
877 optical spin-selection rules are analogous to the NV center in diamond, but involve photons with
878 near-telecom wavelengths. **f)** Rabi oscillation of a single divacancy spin. The high readout
879 contrast of 94% is enabled by resonant excitation of the $|0\rangle \rightarrow |E_y\rangle$ cycling transition. **g)** Room-
880 temperature Rabi oscillations of a single silicon vacancy spin (V_2 center) in 4H-SiC as a function
881 of microwave power.

882 Figures reproduced from: a) b) Ref. ⁵³; c) Ref. ⁶⁰; d) Ref. ⁷²; e) f) Ref. ⁷⁸; g) Ref. ⁷⁵.

883

884 **Figure 3 | Rare-earth ions in crystals and optically-active donors in silicon.**

885 **a)** Fluorescence excitation spectrum of a single Pr^{3+} ion in a YSO microparticle, resolving the
886 hyperfine structure of the $^3\text{P}_0$ excited state ($T = 4$ K). **b)** ODMR for the ground state hyperfine
887 sublevels of a single Pr^{3+} ion in bulk YAG. Readout is achieved by a two-photon upconversion
888 process. The relatively broad ODMR linewidth ($\sim 2\pi \cdot 1.5$ MHz) indicates that the coherence of the
889 Pr^{3+} nuclear spin in YAG is limited by spin-lattice relaxation at 4 K. **c)** ODMR between the electron-
890 nuclear spin singlet (S_0) and triplet (T_-, T_0, T_+) states of an ensemble of singly-ionized ^{77}Se double
891 donors in silicon. Data are taken by first optically pumping the ensemble into the S_0 state and then
892 measuring the relative absorption of the $T \leftrightarrow \Gamma_7$ transition (2902 nm) at 2 K and in Earth's
893 magnetic field ($70 \mu\text{T}$).

894 Figures reproduced from: a) Ref. ⁹¹; c) Ref. ⁹⁵; b) Ref. ¹⁰³.

895

896 **Figure 4 | Quantum registers for quantum networks and computing.**

897 **a)** Photograph showing three lab stations A, B, C at the Delft University of Technology. An
898 entangled state between two NV centers separated by 1.3 km (stations A and B) is generated by
899 sending spin-entangled photons to station C. **b)** Experimental schematic for remote
900 entanglement. Indistinguishable ZPL photons from NV centers at stations A and B are overlapped
901 onto a beam-splitter at station C, where a particular sequence of single photon detections heralds
902 the generation of an entangled state. High-fidelity and fast single-shot spin readout enables a
903 loophole-free test of the Bell inequality. **c)** Principle of entanglement distillation. Two lower quality
904 remote entangled states can produce a single higher fidelity entangled state through local
905 operations and classical communication. **d)** Experimental implementation of entanglement
906 distillation using an NV center electron spin (communication qubit) and a weakly coupled ^{13}C
907 nuclear spin (memory qubit) at each node. The success of the distillation protocol, resulting in a
908 higher fidelity entangled state between the memory qubits, is probabilistic, but is heralded by a
909 particular measurement outcome on the communication qubits. **e)** Scheme for storage of a photon
910 polarization state by the ^{14}N nuclear spin of the NV center. The NV center is first prepared in an
911 electron-nuclear Bell state. At zero magnetic field, the electronic levels $|\pm 1\rangle_e$ and $|A_1\rangle$ form a
912 degenerate Λ system, and the entangled absorption of a resonant photon transfers the photon
913 polarization onto the phase of the nuclear superposition state. Successful absorption is heralded
914 by single-shot spin readout. **f)** Data showing the faithful mapping of the photon polarization onto
915 the nuclear superposition state. **g)** Quantum error correction using a register of three strongly-
916 coupled nuclear spins. This code can surpass the fidelity of no error correction (blue circles) when
917 a single error occurs of one of the qubits (green triangles) or when errors occur with equal
918 probability on all three qubits (red circles).

919 Figures reproduced from: a) b) Ref. ¹¹⁰; c) d) Ref. ¹¹²; e) f) Ref. ¹¹³; g) Ref. ³⁰.

920

921 **Figure 5 | Diverse modalities and applications of quantum sensing with impurity spins.**

922 **a).** Wide-field magnetic imaging of magnetotactic bacteria on top of a dense array of shallow NV
923 centers. The colorbar depicts the magnetic field projection along the [111] NV axis. The inset
924 shows the bright-field image for the same region. **b)** Intracellular temperature map of primary
925 cortical neurons using nanodiamonds (ND) incorporated by cellular uptake. The color code
926 denotes the change in measured temperature for each ND in response to a reduction in
927 environmental temperature. **c)** An atomic force microscope using a diamond scanning tip with a
928 single NV center at its apex enables magnetic field imaging with a spatial resolution of tens of
929 nanometers, determined by the NV to sample distance. **d)** Magnetic stray field image capturing
930 the non-collinear magnetic order of a multiferroic BeFeO₃ thin film. The colorbar is related to the
931 change in local magnetic field from a reference value. **e)** Geometry for NMR on nanoscale sample
932 volumes with a near surface NV magnetic sensor. **f)** NMR chemical shift for ¹⁹F nuclei in PFPE
933 (fomblin) detected by an NV spin. The high spectral resolution of this experiment is achieved by
934 using a long-lived nuclear memory to extend the phase acquisition time.

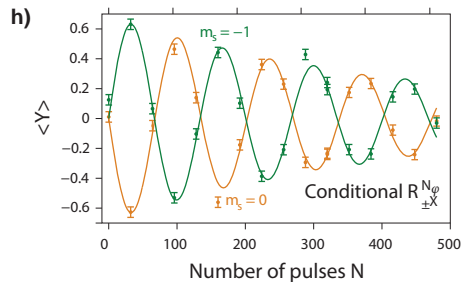
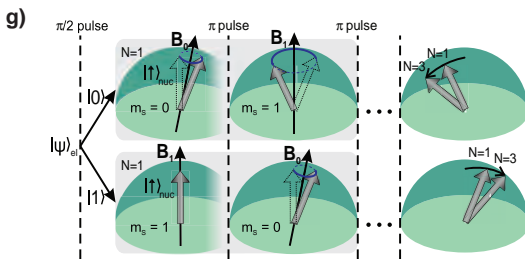
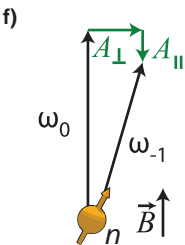
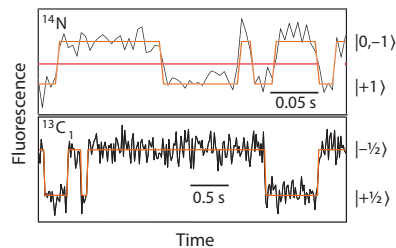
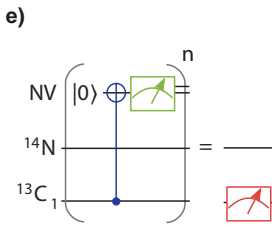
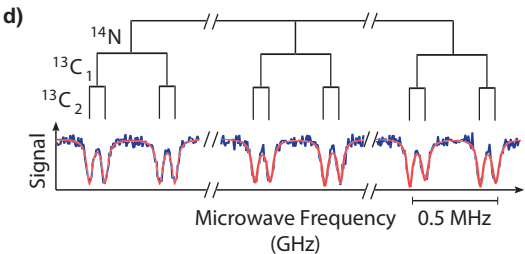
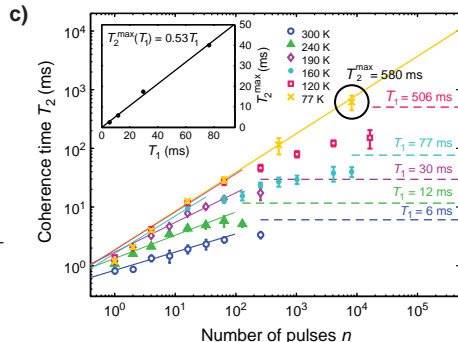
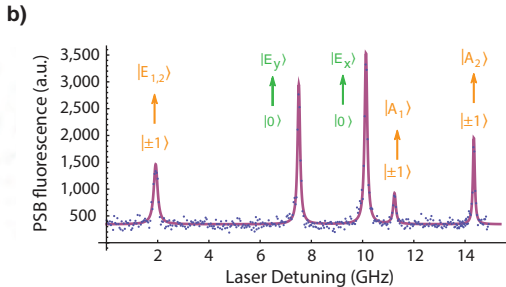
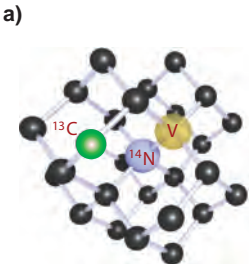
935 Figures reproduced from: a) Ref. ¹²³; b) Ref. ¹²⁴; c) d) Ref. ¹²⁷; e) f) Ref. ¹³⁹.

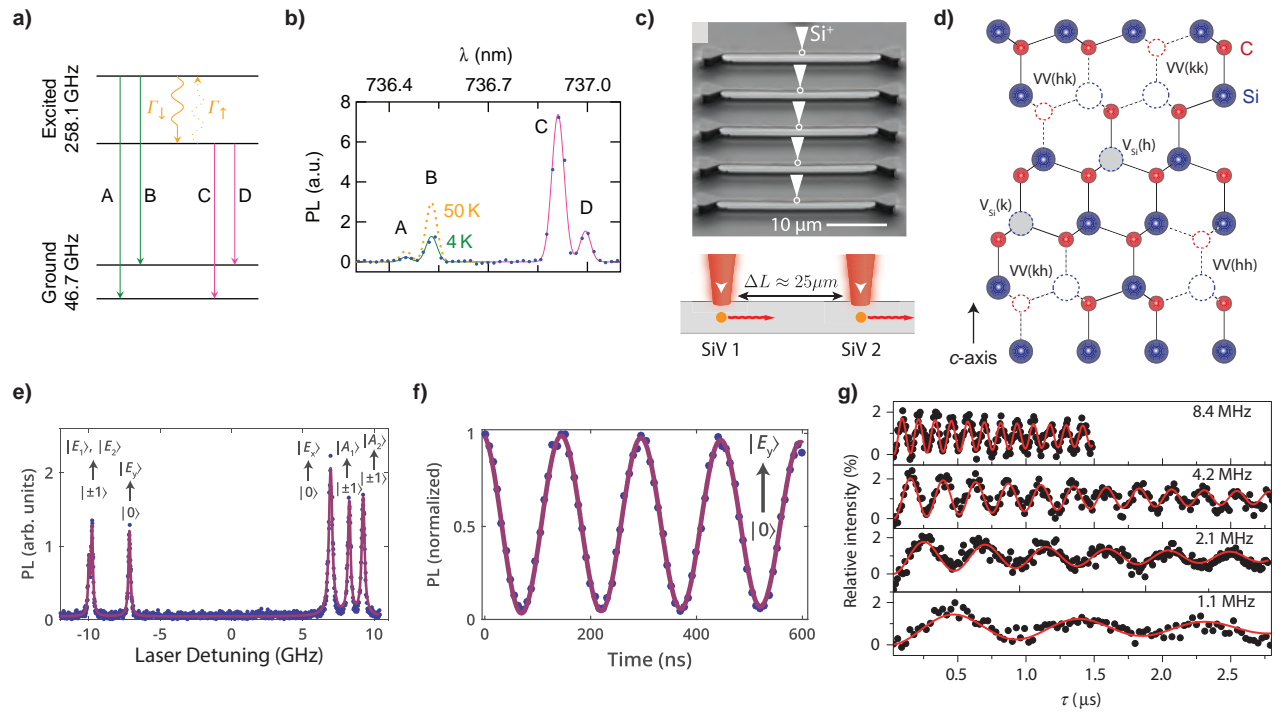
936

937 **Figure 6 | Photonic engineering for solid-state spins.**

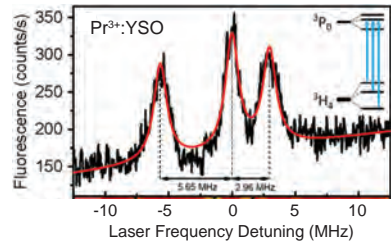
938 **a)** Miniaturized Fabry-Pérot microcavity containing a thin diamond membrane. Nano-positioning
939 a moveable distributed Bragg reflector (DBR) mirror allows *in situ* tuning of the cavity resonance
940 frequency and antinode location. Emission of the NV center into the ZPL is boosted to 46% at 4
941 K. **b)** SEM image of a photonic crystal cavity in 3C-SiC. The starting material is grown as a
942 heteroepitaxial thin film on silicon, allowing for effective substrate removal. Collected PL from a
943 divacancy ensemble in the cavity is enhanced by a factor of 30. **c)** Implementation of a photonic
944 integrated circuit featuring on-chip waveguides and superconducting nanowire single photon
945 detectors. This architecture could provide a route toward scalable, on-chip entanglement of
946 impurity spins.

947 Figures reproduced from: a) Ref. ⁵⁰; c) Ref. ⁸¹; b) Ref. ¹⁴⁸.

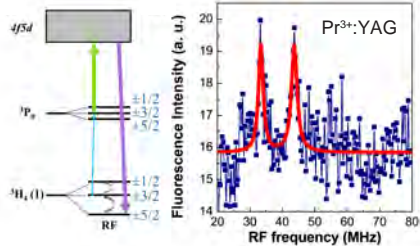




a)



b)



c)

